

# Boundary-Layer Meteorology

## Surface temperature and surface layer turbulence in a convective boundary layer

--Manuscript Draft--

<b>Manuscript Number:</b>	
<b>Full Title:</b>	Surface temperature and surface layer turbulence in a convective boundary layer
<b>Article Type:</b>	Research Article
<b>Keywords:</b>	Infra-red imagery; Surface layer; Surface layer plumes; Surface temperature
<b>Corresponding Author:</b>	Jan Kleissl, Ph.D. University of California, San Diego La Jolla, CA UNITED STATES
<b>Corresponding Author Secondary Information:</b>	
<b>Corresponding Author's Institution:</b>	University of California, San Diego
<b>Corresponding Author's Secondary Institution:</b>	
<b>First Author:</b>	Anirban Garai
<b>First Author Secondary Information:</b>	
<b>Order of Authors:</b>	Anirban Garai Jan Kleissl, Ph.D. Eric Pardyjak Marie Lothon Gert-Jan Steeneveld
<b>Order of Authors Secondary Information:</b>	
<b>Abstract:</b>	<p>Previous laboratory and atmospheric experiments have shown that turbulence influences the surface temperature in a convective boundary layer. The main objective of this study is to examine land-atmosphere coupled heat transport mechanism for different stability conditions. High frequency infrared imagery and sonic anemometer measurements were obtained during the Boundary Layer Late Afternoon and Sunset Turbulence experimental campaign. Temporal turbulence data in the surface layer are then analyzed jointly with spatial surface temperature imagery.</p> <p>The surface temperature structures are strongly linked to atmospheric turbulence as manifested by several findings. The surface temperature coherent structures move at an advection speed similar to the upper surface layer or mixed layer wind speed with a decreasing trend with stability. Also, with increasing instability the streamwise surface temperature structure size decreases and the structures become more circular. The sequencing of surface and air temperature patterns is further examined through conditional averaging. Surface heating causes the initiation of warm ejection events followed by cold sweep events that result in surface cooling. The ejection events occur about 25% of the time, but account for 60 to 70% of the total sensible heat flux and cause fluctuations of up to 30% in the ground heat flux. Cross-correlation analysis between air and ground temperature confirms the validity of scalar footprint models.</p>
<b>Suggested Reviewers:</b>	<p>Gabriel Katul, PhD Professor, Duke University gaby@duke.edu Conducted ground-breaking study in 1998 on the same topic, albeit limited to a single 'pixel'.</p> <p>Christopher Jeffery, PhD Staff Scientist, Los Alamos National Lab cjeffery@lanl.gov Lead Balick et al. study that had similar objectives as our experiment.</p>

	<p>James A Voogt, PhD Professor, University of Western Ontario javoogt@uwo.ca Studied surface temperature fluctuations characteristics in an urban environment.</p>
	<p>Andreas Christen , PhD Assistant Professor, University of British Columbia andreas.christen@ubc.ca Studied surface temperature characteristics in an urban environment</p>
	<p>Kyaw Tha Paw U, PhD Professor, University of California, Davis ktpawu@ucdavis.edu Expert in Surface Renewal analysis</p>



## 10 Abstract

11 Previous laboratory and atmospheric experiments have shown that turbulence influences the  
12 surface temperature in a convective boundary layer. The main objective of this study is to examine  
13 land-atmosphere coupled heat transport mechanism for different stability conditions. High frequency  
14 infrared imagery and sonic anemometer measurements were obtained during the Boundary Layer Late  
15 Afternoon and Sunset Turbulence experimental campaign. Temporal turbulence data in the surface  
16 layer are then analyzed jointly with spatial surface temperature imagery.

17 The surface temperature structures are strongly linked to atmospheric turbulence as  
18 manifested by several findings. The surface temperature coherent structures move at an advection  
19 speed similar to the upper surface layer or mixed layer wind speed with a decreasing trend with  
20 stability. Also, with increasing instability the streamwise surface temperature structure size decreases  
21 and the structures become more circular. The sequencing of surface and air temperature patterns is  
22 further examined through conditional averaging. Surface heating causes the initiation of warm  
23 ejection events followed by cold sweep events that result in surface cooling. The ejection events occur  
24 about 25% of the time, but account for 60 to 70% of the total sensible heat flux and cause fluctuations  
25 of up to 30% in the ground heat flux. Cross-correlation analysis between air and ground temperature  
26 confirms the validity of scalar footprint models.

27 Keywords: Infra-red imagery, Surface layer, Surface layer plumes, Surface temperature.

## 28 1. Introduction

29 The fluid temperature trace in turbulent heat transfer over a flat surface shows the  
30 characteristics of periodic activities comprised of alternating large fluctuations and periods of  
31 quiescence (Townsend, 1959; Howard, 1966). Sparrow et al. (1970) observed that these periodic  
32 activities are due to mushroom-like structures of ascending warm fluid caused by instability due to  
33 buoyant forcing (Howard, 1966). Similar structures consisting of ascending warm fluid are also  
34 observed in the surface layer of a convective boundary layer (CBL) and known as surface layer  
35 plumes. These plumes have diameters on the order of the surface layer height, advection velocities  
36 close to the average wind speed over their depth, are tilted by about  $45^{\circ}$  due to wind shear, and are  
37 responsible for a majority of total momentum and heat transport (Kaimal and Businger, 1970;  
38 Wyngaard et al. 1971; Kaimal et al. 1976; Wilczak and Tillman, 1980; Wilczak and Businger, 1983;  
39 Renno et al. 2004). As these plumes ascend through the CBL, they combine with each other to create  
40 thermals in the mixed layer.

41 Conditional averaging of the surface layer plumes by Schols (1984) and Schols et al. (1985)  
42 revealed that the resulting air temperature trace shows ramp-like patterns. Gao et al. (1989), Paw U et  
43 al. (1992), Braaten et al. (1993) and Raupach et al. (1996) studied these temperature ramp patterns  
44 over different canopies and modelled the transport process using the surface renewal (SR) method.  
45 The SR method conceptualizes the heat exchange process to occur based on coherent structures: a  
46 cold air parcel descends to the ground during the sweep event, as it remains close to the ground it is  
47 heated, and when it achieves sufficient buoyancy the warm air parcel ascends during the ejection  
48 event. The SR method has been successfully employed to estimate sensible and latent heat flux over  
49 different canopies by Paw U et al. (1995), Snyder et al. (1996), Spano et al. (1997, 2000), Castellvi et  
50 al. (2002), Castellvi (2004) and Casstellvi and Snyder (2009).

51 The effect of coherent structures on surface temperature (ST) was first observed by Derksen  
52 (1974) and Schols et al. (1985) who found streaky patterns of ST with about a  $2^{\circ}\text{C}$  heterogeneity  
53 along the wind direction using an airborne thermal infra-red (IR) camera. Hetsroni and Rozenblit  
54 (1994), Hetsroni et al. (2001), and Gurka et al. (2004) observed a similar streaky structure of ST in a  
55 laboratory convective water flume experiment at different Reynolds numbers. High ST streaks  
56 corresponded to low velocity fluid streaks in the boundary layer and the distance between streaks  
57 increased with Reynolds number. Using an IR temperature sensor Paw U et al. (1992), Katul et al.  
58 (1998) and Renno et al. (2004) observed ST fluctuations in the CBL with an amplitude of  $0.5^{\circ}\text{C}$  over  
59 2.6 m high maize crops, greater than  $2^{\circ}\text{C}$  over 1 m high grass, and  $2\text{-}4^{\circ}\text{C}$  over a desert area,  
60 respectively. Using IR imagery, Ballard et al. (2004), Vogt (2008) and Christen et al. (2012) observed  
61 spatial heterogeneities in the magnitude of ST fluctuations over a grass canopy, a bare field, and in an  
62 urban environment, respectively.

63 Direct numerical simulation of turbulent heat transfer coupled with heat conduction in the  
64 adjacent solid by Tiselj et al. (2001) revealed that the magnitude of ST fluctuation depends on the  
65 wall thickness and relative strength of thermal response times for the solid and fluid. Balick et al.  
66 (2003) identified similar key parameters for the coupled heat transfer process at the earth's surface.  
67 Ballard et al. (2004) hypothesized that high frequency ST fluctuations are caused by turbulent mixing.  
68 Katul et al. (1998) and Renno et al. (2004) argued that ST fluctuations are caused by inactive eddy  
69 motion and convective mixed layer processes. Christen and Voogt (2009, 2010) visualized the spatial  
70 ST field in a suburban street canyon and qualitatively attributed the vertical heat transport to the  
71 observed coherent structures that were shown to move along the wind direction.

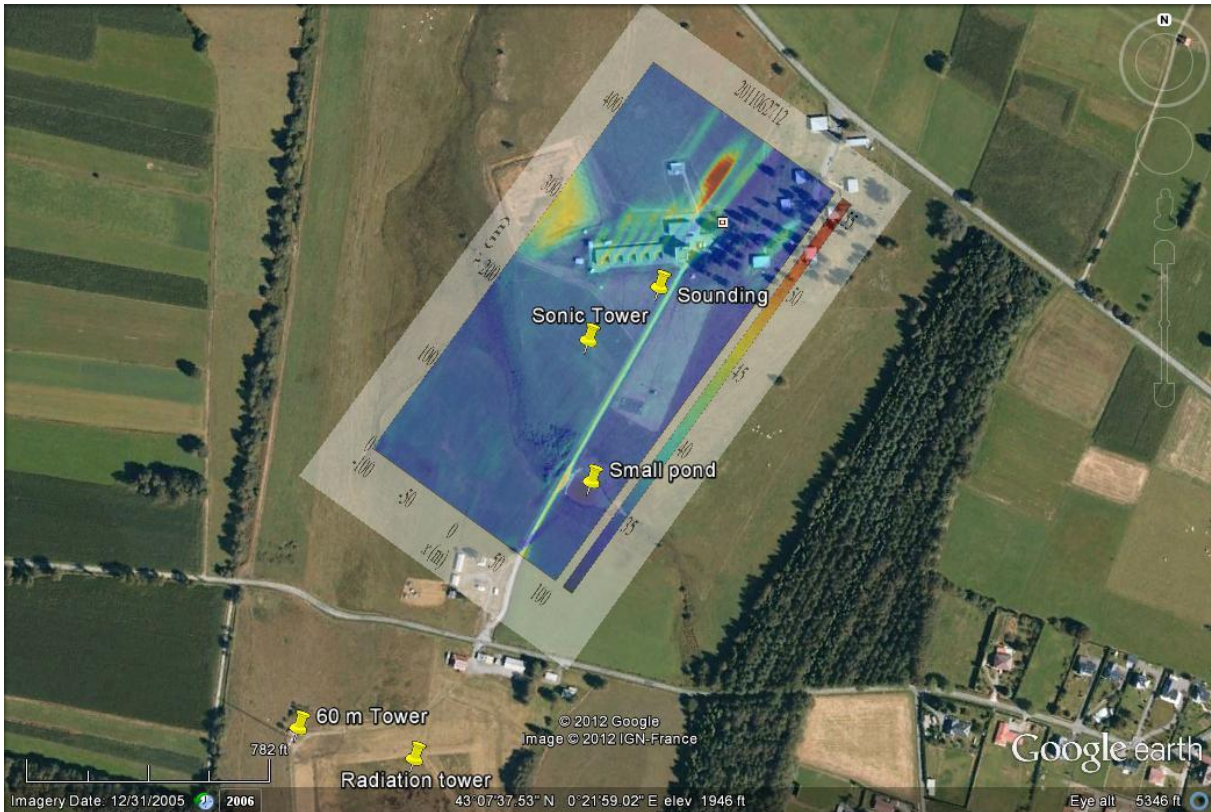
72 Garai and Kleissl (2011) examined ST structures and heat transport processes over an  
73 artificial turf field using 1 Hz IR imagery. Although the camera footprint was smaller (48 m x 15 m)  
74 than the scale of the largest ST structures, different ST characteristics were identified corresponding  
75 to different phases of the SR process. The ST field showed large cold structures during sweep events,  
76 small patches of warm structures in a cold background during the transition from sweep to ejection,  
77 large warm structures during the ejection events and small patches of cold structures in a warm  
78 background during the transition from ejection to sweep. Sequential animation of the ST showed  
79 growth and merging of thermal footprints as they move along the wind direction. The main objective  
80 for the experimental setup was to address the main limitation of Garai and Kleissl (2011) and resolve  
81 the largest ST structures by increasing the mounting height of the IR camera. Furthermore turbulence  
82 measurements were collocated at different heights that allowed further investigating the cause and  
83 manifestation of ST structures as a function of atmospheric stability and the interaction between  
84 thermal footprints and lower surface layer turbulence. In Sections 2, 3, and 4 we will describe the  
85 experimental setup, results, and discussion and conclusions, respectively.

## 86 2. Experiment and data processing

### 87 a. Experimental setup

88 The experiment was conducted in collaboration with Boundary Layer Late Afternoon and  
89 Sunset Turbulence (BLLAST; Lothon et al., 2012) field campaign at Centre de Recherches  
90 Atmosphériques, Lannemezan, France from 14 June to 8 July, 2011 (Figure 1). ST data at 1 Hz were  
91 captured by a FLIR A320 Thermal IR camera. It was mounted 59 m above ground level (a.g.l.) at the  
92 60 m tower (43°07'25.15" N, 0°21'45.33" E) looking towards 55° N with an inclination of 2° from 16  
93 June to 29 June, 2011. It overlooked a 9 cm high grass field with an albedo of 0.19. Longwave  
94 radiation (8 – 14  $\mu\text{m}$  wavelength) from the surface was measured in 240 x 320 pixels and converted  
95 into ST ( $T_s$ ) assuming an emissivity of 0.95 (Oke, 1987). The accuracy of the camera is 0.08 K. A  
96 coordinate system transformation and interpolation was performed to transform the original image to

97 a cartesian coordinate system. This resulted in a camera footprint of 450 m x 207 m with a uniform  
98 resolution of 4.5 m x 0.65 m. A 1 hr daytime average of the ST from the IR camera (overlaid on a  
99 map in Figure 1) shows road, buildings and bare soil regions to be warmer and a small pond to be  
100 cooler than the grass regions.



101

102 Figure 1. Google Earth map of the experimental site. The locations of the 10 m sonic anemometer  
103 tower, 60 m tower, radiation tower, and release position of radiosondes are marked. 1-hr averaged ST  
104 as viewed from the 60 m tower at 1200 - 1259 UTC (1400 -1459 local time) on 27 June, 2011 is  
105 overlaid. The quantitative analysis considers only the area of  $y < 275$  m.

106 Four Campbell Scientific Sonic Anemometer-Thermometers (CSAT) measured turbulent  
107 velocity ( $u$ ,  $v$ ,  $w$ ) and sonic air temperature ( $AT$ ,  $T_a$ ) at 20 Hz at 2.23 m, 3.23 m, 5.27 m and 8.22 m  
108 a.g.l. inside the camera footprint at  $43^{\circ}07'39.2''$  N,  $0^{\circ}21'37.3''$  E (“Sonic Tower” in Fig. 1).  
109 Hereinafter these CSATs will be referred to as 2 m, 3 m, 5 m and 8 m CSATs. The CSATs were  
110 pointing towards  $60^{\circ}$  N. A coordinate system rotation was conducted to ensure  $|\langle w \rangle / M| < 1\%$   
111 (angled brackets denote temporal averaging and  $M$  is the horizontal wind speed) and to orient the  
112 CSAT winds into the IR-camera coordinate system following Wilczak et al. (2001).

113 Radiosondes were released at  $43^{\circ}07'41''$  N,  $0^{\circ}22'01''$  E (“Sounding” in Fig. 1) every 6 hours  
114 until 25<sup>th</sup> June, 2011 and every 3 hours thereafter providing profiles of wind speed, direction,  
115 temperature, humidity up to 20 km with a vertical resolution of 5 m.

116 A radiation tower at 43°07'26" N, 0°21'50.4" E near the 60 m tower (Figure 1) was equipped  
 117 with Kipp & Zonen CM22 and CM21 pyranometers to measure the shortwave up- and down-welling  
 118 irradiances, and an Eppley-PIR and a Kipp & Zonen CG4 pyrgeometers to measure the longwave up-  
 119 and down-welling irradiance respectively. All radiation measurements were reported as 1 min  
 120 averages.

121 All measurement platforms were GPS synchronized to Coordinated Universal Time (UTC),  
 122 which lags local time by 2 hours.

## 123 b. Data processing

124 Ogive tests (Foken et al., 2006) revealed that an averaging period of 5-min is sufficient to  
 125 estimate momentum and heat fluxes from the 2 m to 8 m CSATs using the eddy covariance method  
 126 (for details see Appendix). To minimize the effects of changing meteorological conditions on the  
 127 fluctuating time series of wind speed ( $u$ ,  $v$ ,  $w$ ), AT ( $T_a$ ), and ST ( $T_s$ ) the 5-min linear trend was  
 128 removed using:

$$129 \quad X' = X(t) - (\langle X \rangle_{5min} - a_{X,5min} t), \quad (1)$$

130 where  $a_{X,5min}(t)$  is the linear time dependence coefficient of variable  $X$  (for ST,  $a_{ST,5min}(t, x, y)$ , i.e. it is  
 131 computed separately for each camera pixel). Since, there were no continuously functioning finewire  
 132 thermocouples or infra-red gas analyzers on the Sonic tower, the kinematic sensible heat flux was

133 estimated using  $\frac{H}{\rho_a c_{p,a}} \approx \frac{\langle w' T_a' \rangle}{(1+0.06/B)}$ , where  $\rho_a$ ,  $C_{p,a}$  and  $B$  are the dry air density, dry air specific heat

134 and the Bowen ratio estimated using a CSAT and a LICOR 7500A CO<sub>2</sub>/H<sub>2</sub>O analyzer mounted at  
 135 29.3 m a.g.l. at the 60 m tower, operated at 10 Hz, and taking an averaging period of 10 min. The 2 m  
 136 CSAT data was used to estimate mean sensible heat flux ( $H$ ), friction velocity  $u_* = (\langle u'w' \rangle^2 +$

137  $\langle v'w' \rangle^2)^{1/4}$ , convective velocity  $w_* = \left( \frac{gz_i}{\langle T_a \rangle \rho_a c_{p,a}} \frac{H}{\rho_a c_{p,a}} \right)^{1/3}$ , surface layer temperature scale  $T_*^{SL} =$

138  $-\frac{H}{\rho_a c_{p,a} u_*}$ , Obukhov length  $L = -\frac{\langle T_a \rangle u_*^3}{\kappa g \rho_a c_{p,a}}$  and flux Richardson number  $Ri_f = \frac{g}{u_*^2} \frac{H}{\rho_a c_{p,a} \frac{\partial \langle M \rangle}{\partial z}}$ , where  $\kappa$  and

139  $g$  are von Karman constant and gravitational constant respectively. The vertical gradient of horizontal  
 140 wind speed was estimated using Businger-Dyer similarity relationships.

141 Footprint functions estimate the relative contribution of scalar sources from different ground  
 142 locations to the measurement location of the scalar. To calculate footprints of different CSATs, we  
 143 used the scalar footprint derived from the flux footprint model by Hsieh et al. (2000). In this model  
 144 the 1-D flux footprint function ( $f$ ) for the unstable boundary layer is

$$145 \quad f(\tilde{x}, z_m) = \frac{1}{\kappa^2 \tilde{x}^2} 0.28 z_u^{0.59} |L|^{1-0.59} \exp\left(\frac{-1}{\kappa^2 \tilde{x}} 0.28 z_u^{0.59} |L|^{1-0.59}\right), \quad (2a)$$



146 where  $\tilde{x}$ ,  $z_m$  and  $z_u$  are streamwise distance from the measurement tower, measurement height and a  
 147 scaled measurement height defined as  $z_u = z_m(\log(Z_m/z_o) - 1 + z_o/z_m)$ , where  $z_o$  is the roughness  
 148 height. The flux footprint ( $f$ ) is related to scalar footprint ( $C$ ) by (Kormann and Meixner, 2001)

$$149 \quad M \frac{\partial C}{\partial \tilde{x}} = - \frac{\partial f}{\partial z}. \quad (2b)$$

150 The 1-D scalar footprint function ( $C$ ) was then used to calculate the 2-D scalar footprint function  
 151 ( $C_{2D}$ ) assuming a Gaussian distribution of zero mean and standard deviation of the wind direction ( $\sigma_\theta$ )  
 152 using

$$153 \quad \sigma_{\tilde{y}} = \frac{\sigma_\theta \tilde{x}}{1 + \sqrt{\frac{\tilde{x}}{400(M)}}},$$

$$154 \quad C_{2D} = \frac{C}{\sqrt{2\pi}\sigma_{\tilde{y}}} e^{-\frac{\tilde{y}^2}{2\sigma_{\tilde{y}}^2}}, \quad (2c)$$

155 where  $\tilde{y}$  is spanwise distance. For the comparison of 20 Hz turbulence data with 1 Hz footprint  
 156 averaged ST data, a box filter of size 1 s centred at the time stamp of ST was applied.

157 Net radiation  $R_{net}$  was obtained from the radiation tower measurements, but up-welling  
 158 longwave irradiance measured at the radiation tower was replaced by the average IR-camera  
 159 measurement.

160 Finally, the surface heat flux  $G$  was modelled numerically by solving the transient 3-D heat  
 161 conduction equation:

$$162 \quad \frac{\partial T_g}{\partial t} = \alpha_g \left( \frac{\partial^2 T_g}{\partial x^2} + \frac{\partial^2 T_g}{\partial y^2} + \frac{\partial^2 T_g}{\partial z^2} \right), \quad (3a)$$

163 where  $\alpha_g$  and  $T_g$  are the thermal diffusivity and the temperature of the soil respectively. The  
 164 conduction equation was discretized horizontally using a spectral method with periodic boundary  
 165 conditions; vertically a second order finite difference scheme was used; the Euler implicit scheme was  
 166 applied for time integration. The numerical solution of Eq. 3a was validated against the analytical  
 167 solution of constant and sinusoidal varying surface temperature (not shown). To simulate soil  
 168 temperatures, homogeneous clay soil with 40% volumetric water content was assumed yielding  
 169 thermal diffusivity  $\alpha_g$  and conductivity  $k_g$  of  $0.4 \text{ mm}^2 \text{ s}^{-1}$  and  $0.8 \text{ W m}^{-1} \text{ K}^{-1}$  respectively (Campbell  
 170 and Norman, 1998). The IR temperature ( $T_s$ ) was used as top-surface boundary condition ( $z = 0 \text{ m}$ ), an  
 171 adiabatic boundary condition ( $\frac{\partial T_g}{\partial z} = 0$ ) was used as the bottom boundary condition ( $z = -5.5 \text{ m}$ ) and

172 the temperature in the domain was initiated by  
 173  $T_g(x, y, z, t = 0) = T_\infty + \frac{\langle G \rangle}{k_g} \left\{ 2 \left( \frac{\alpha_g \tau}{\pi} \right)^{1/2} \exp\left(-\frac{z^2}{4\alpha_g \tau}\right) + \frac{z}{2} \operatorname{erfc}\left(-\frac{z}{2\sqrt{\alpha_g \tau}}\right) \right\}$ , where  $\langle G \rangle$  ( $= R_{net} -$

174  $(1 + \frac{1}{B})H$  ) is the mean surface heat flux obtained from the surface energy balance,  $\tau$   
 175  $(= \left[ \frac{k_g((T_s) - T_\infty)}{2(G)} \right]^2 \frac{\pi}{\alpha_g})$  is a dummy time variable to ensure minimal unrealistic initialization effect  
 176 (Carslaw and Jaeger, 1959),  $T_\infty$  (= 288 K) is the soil temperature at  $z \rightarrow -\infty$  (corresponding to the  
 177 annual average air temperature) and erfc is complimentary error function. As the temperature gradient  
 178 is strongest near the surface, the vertical grid resolution was set to 1.5 mm; below  $z = -0.05$  m the  
 179 vertical grid was stretched uniformly to 0.1 m resolution. The simulation was spun up for 100 time  
 180 steps to limit the influence of the initial conditions. The heat flux at the surface was then computed  
 181 from  $T_g$  as:

$$182 \quad G = \left[ \frac{\Delta z}{2\Delta t} \int_{\Delta t} \rho_g C_{p,g} \frac{\partial T_g}{\partial t} dt \right] - \left[ \frac{\Delta z}{2\Delta x} \int_{\Delta x} k_g \frac{\partial^2 T_g}{\partial x^2} dx + \frac{\Delta z}{2\Delta y} \int_{\Delta y} k_g \frac{\partial^2 T_g}{\partial y^2} dy \right] + \left[ k_g \frac{T_s - T_{g,-\Delta z}}{\Delta z} \right], \quad (3b)$$

183 where  $\rho_g$ ,  $C_{p,g}$ ,  $\Delta x$ ,  $\Delta y$ ,  $\Delta z$  are density, specific heat of the soil and grid size in horizontal ( $x$ ,  $y$ ) and  
 184 vertical ( $z$ ) directions respectively. In Eq. 3b the first, second and third bracketed terms represent  
 185 temporal storage, horizontal heat diffusion and vertical heat diffusion respectively.

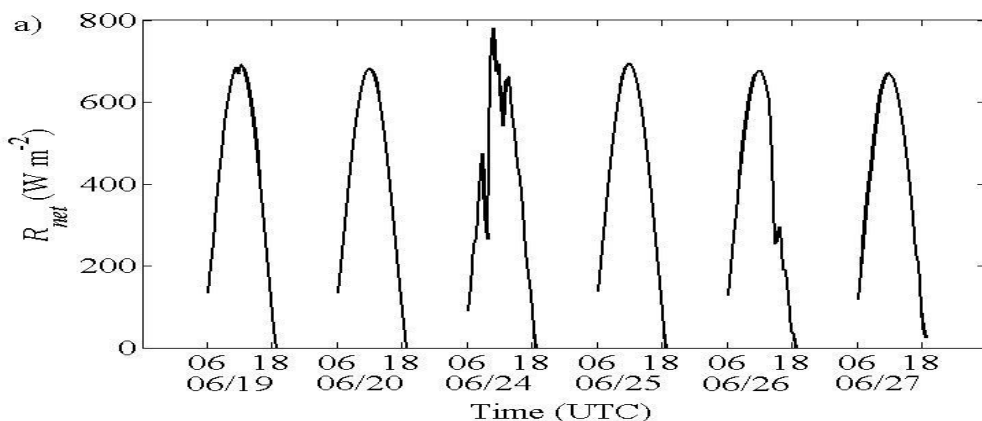
### 186 3. Results

187 Since ST fluctuations exceed the noise level of the camera only during unstable conditions  
 188 (Garai & Kleissl 2011), only daytime data were considered for detailed analysis. Building ( $y > 275$  m)  
 189 and road (a straight line from  $x = 65$  m at  $y = 0$  m to  $x = 30$  m at  $y = 300$  m) pixels (Fig. 1) in the IR  
 190 images were omitted from the analysis, to minimize effects of surface heterogeneity.

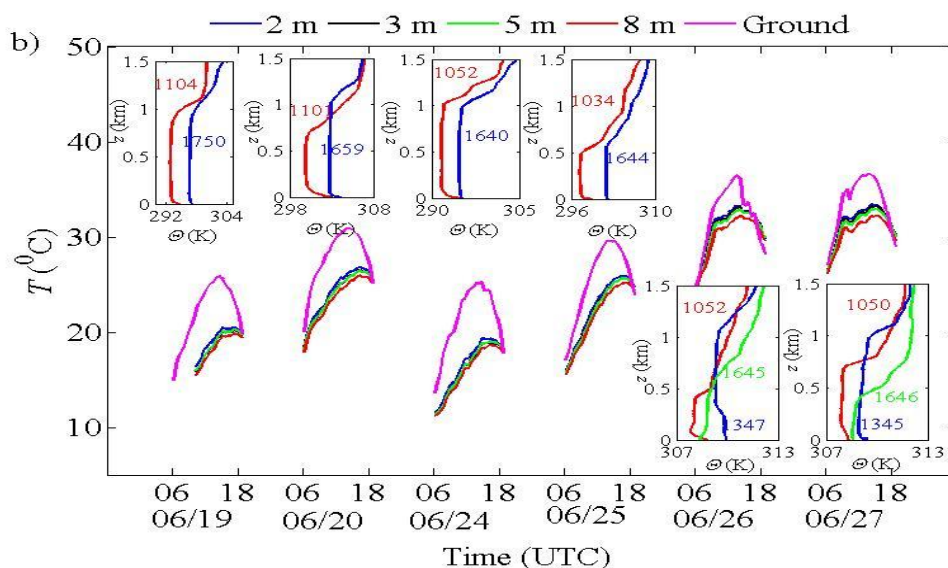
#### 191 a. Meteorological conditions

192 Figure 2 presents 30-min averaged meteorological conditions for the intensive observational  
 193 periods consisting of the clear days during 16 to 27 June, 2011. Potential temperature from radiosonde  
 194 data are shown in the inset of the figures. Clear days are expected to produce both stationary time  
 195 periods and the most unstable stability conditions.  $R_{net}$  reaches up to  $700 \text{ W m}^{-2}$  during midday for all  
 196 clear days. There were some early morning and late afternoon clouds on 24 and 26 June, respectively.  
 197 Rain (about 2-2.5 mm) occurred on 18 and 22-23 June as cold low pressure systems from the Atlantic  
 198 Ocean crossed the site. AT dropped to 15-20 °C just after the rain and increased on successive clear  
 199 days. ST followed a similar trend as AT. Potential temperature ( $\theta$ ) profiles from radiosondes show  
 200 that the inversion height ( $z_i$ ) did not exhibit a strong diurnal cycle except on 20, 26 and 27 June. It was  
 201 about 1 km for 19 and 24 June and 600 m for 25 June. It increased from 750 m to 1 km on 20 June,  
 202 increased from 500 m to 1 km and then dropped to 750 m on 26 June and increased from 750 m to 1  
 203 km and then dropped to 450 m on 27 June for the 1050, 1350, and 1650 UTC soundings, respectively.  
 204 The near surface wind speed was about  $2.5 \text{ m s}^{-1}$  for 19, 20 and 24 June and about  $3 \text{ m s}^{-1}$  for 25 to 27

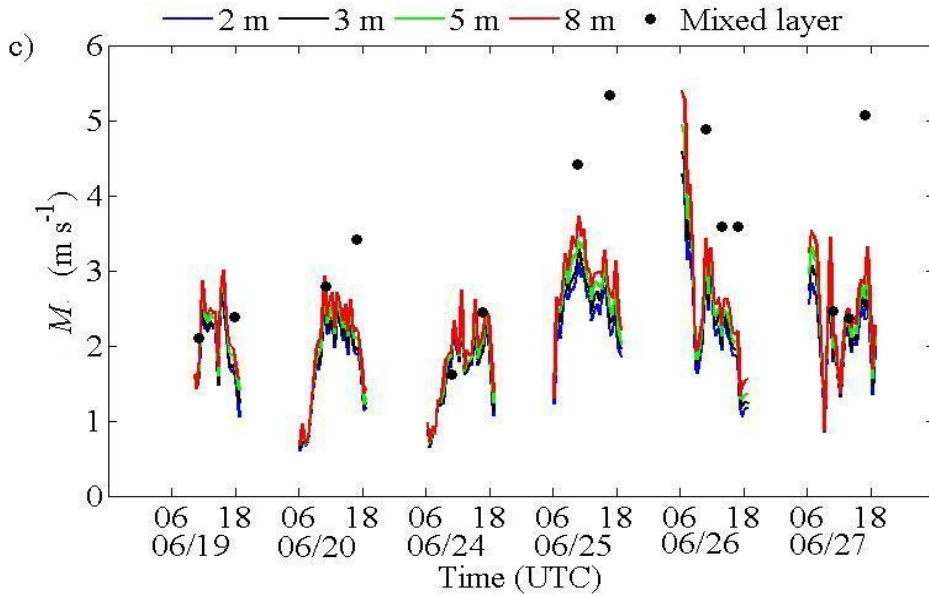
205 June. Mixed layer wind speed (the mean of radiosonde data from  $z/z_i = 0.1$  to 0.8) was close to the 8  
 206 m wind speed for all days except 25 and 26 June, when the mixed layer wind speed was at least 25%  
 207 larger. Wind direction was northerly for 19 and 24 June, easterly for 25 and 26 June and north-  
 208 easterly for 20 and 27 June. Easterly to north-easterly wind is typical for the mountain-plain  
 209 circulation in the area.



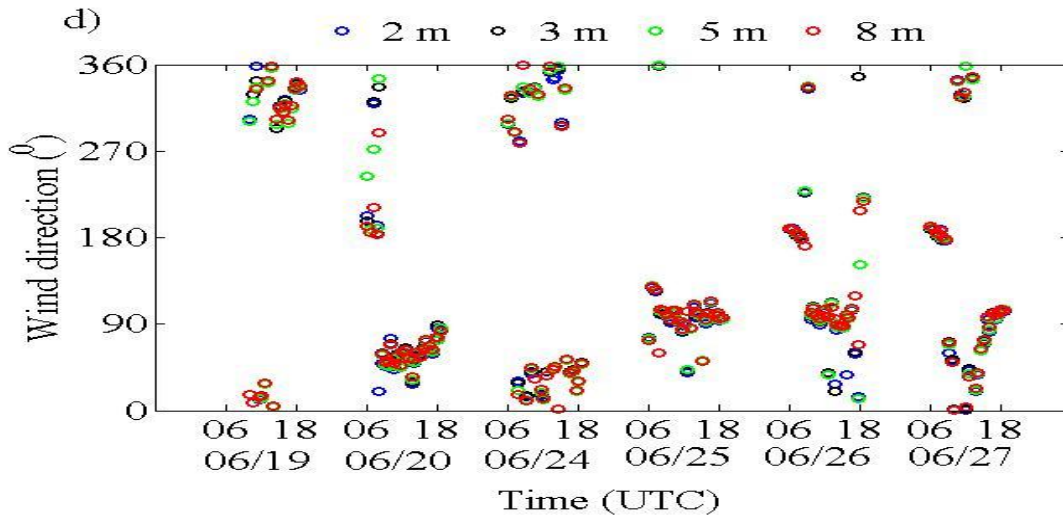
210



211



212



213

214 Figure 2. 30-min averages of (a) net radiation, (b) temperatures, (c) wind speed and (d) wind  
 215 direction. Radiosonde potential temperature profiles are shown in the inset of (b), where the release  
 216 time (HHMM UTC) is shown in colour.

217 Thirty minute periods were chosen for further investigation based on the following stationary  
 218 criteria applied to the 2 m CSAT data: constant Obukhov length and wind speed (standard deviation  
 219 of the six 5 min means within a half hour less than 10% of the mean) and constant wind direction  
 220 (standard deviation of the six 5 min vector means less than  $20^\circ$ ). Data from the days after the rain (19  
 221 and 24 June) are excluded, as the IR surface temperature is affected by local pooling of water.  
 222 Stationary periods are characterized in Table 1 in order of increasing stability. The gradient  
 223 Richardson number is strongly correlated with the stability parameter,  $\zeta = z/L$  (Businger et al. 1971),  
 224 which in turn is related to the flux Richardson number by the ratio of turbulent diffusivity of heat and  
 225 momentum for unstable boundary layers. The data from the 2 m CSAT, indicate that  $Ri_f = 1.69\zeta$  with

226 99.7% coefficient of determination, where  $\zeta = 2.23 \text{ m/L}$ . Thus, either  $\zeta$  or  $Ri_f$  can be used to  
 227 investigate the impact of stability on the different turbulent statistics. For the remainder of the paper  
 228 stability will be parameterized by  $\zeta$ .

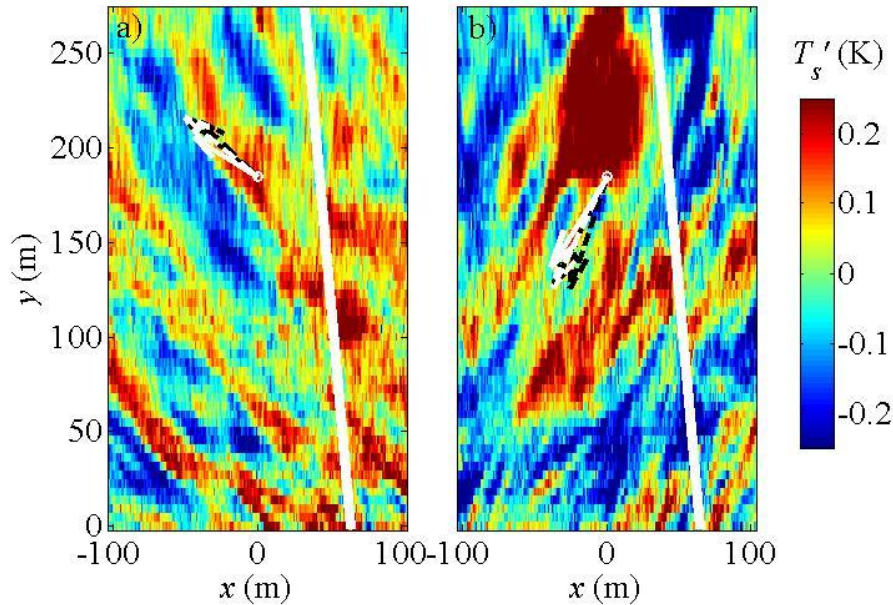
229 Table 1. Scales, stability and turbulence parameters sorted by  $L$  and  $Ri_f$  during periods classified as  
 230 stationary (see text for criteria used). Inversion heights  $z_i$  were estimated visually from the radio  
 231 soundings as inflection point in the potential temperature profiles (increase in potential temperature  
 232 exceeds 1 K over 100 m height).

Time (UTC)	$L$ (m)	$Ri_f$ (-)	$u_*$ (m s <sup>-1</sup> )	$w_*$ (m s <sup>-1</sup> )	$\frac{H}{\rho_a c_{p,a}}$ (K m s <sup>-1</sup> )	$z_i$ (km)
0930-1000, 27 June	-5.49	-0.66	0.15	0.95	0.045	0.6
0830-0900, 26 June	-6.68	-0.52	0.15	0.71	0.028	0.4
1100-1130, 20 June	-7.27	-0.47	0.22	1.38	0.113	0.7
1100-1130, 27 June	-8.45	-0.39	0.19	1.15	0.058	0.8
1030-1100, 27 June	-8.45	-0.39	0.18	1.06	0.053	0.7
1530-1600, 20 June	-8.84	-0.37	0.19	1.31	0.062	1.1
0935-1005, 26 June	-9.40	-0.35	0.17	0.82	0.043	0.4
0825-0855, 27 June	-10.22	-0.31	0.15	0.76	0.027	0.5
1200-1230, 25 June	-11.74	-0.27	0.26	1.23	0.112	0.5
1030-1100, 25 June	-12.49	-0.25	0.27	1.23	0.112	0.5
0900-0930, 25 June	-14.33	-0.21	0.27	1.18	0.098	0.5
1000-1030, 25 June	-14.73	-0.20	0.28	1.22	0.109	0.5
0830-0900, 25 June	-15.60	-0.19	0.26	1.10	0.079	0.5
1000-1030, 26 June	-19.46	-0.15	0.22	0.81	0.042	0.4
1115-1145, 26 June	-19.49	-0.15	0.24	1.00	0.053	0.6
1530-1600, 25 June	-19.61	-0.15	0.23	0.93	0.049	0.5
1000-1030, 27 June	-22.32	-0.13	0.26	1.10	0.059	0.7
1130-1200, 26 June	-22.81	-0.12	0.25	0.98	0.049	0.6
1130-1200, 25 June	-23.57	-0.12	0.33	1.25	0.117	0.5
1700-1730, 20 June	-36.49	-0.07	0.21	0.88	0.019	1.1
1025-1055, 26 June	-37.23	-0.07	0.29	0.87	0.051	0.4

233

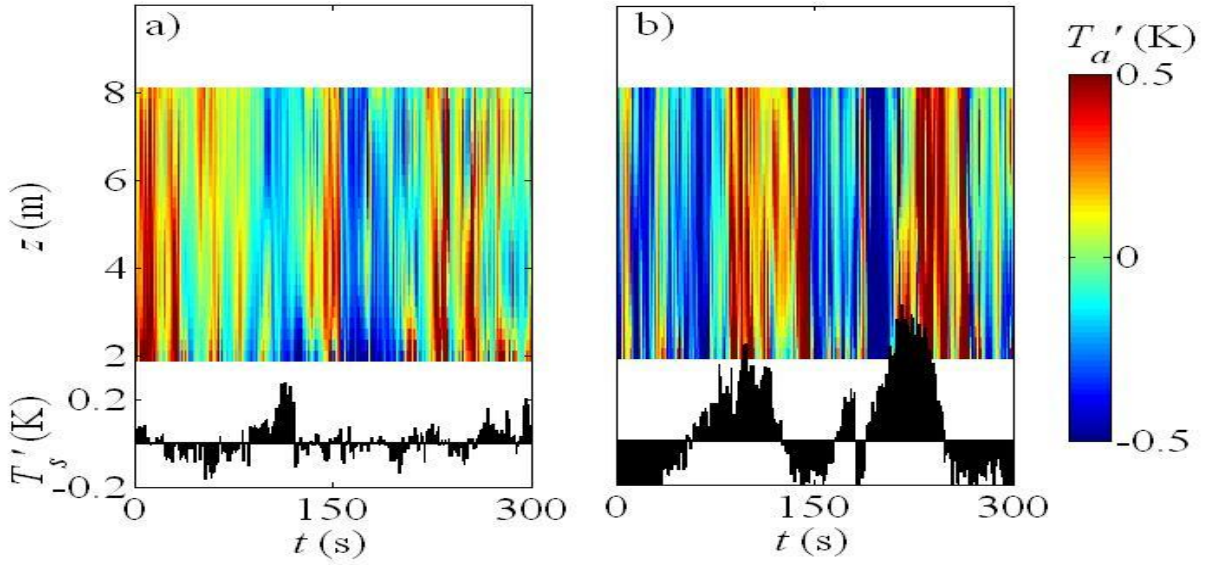
234 b. Spatial and temporal evolution of surface and air temperatures and  
 235 comparison to similarity functions

236 We have chosen the time periods with  $L = -10.22$  m and  $-19.49$  m to illustrate stability  
 237 dependence, as they are representative of more unstable and less unstable conditions in our dataset  
 238 and of different wind directions ( $177^\circ$  for  $L = -10.22$  m and  $91^\circ$  for  $L = -19.49$  m). Structures in the  
 239 spatial ST fluctuation field are aligned with the wind direction (Fig. 3) demonstrating that the  
 240 observed ST structures are not an artifact of surface heterogeneity or topography (since temporal  
 241 averages have been removed as in Eq. 1). With time these ST structures grow, merge with each other,  
 242 and move along with the wind (not shown).



243  
 244 Figure 3. Snapshots of ST fluctuations for  $L =$  a)  $-10.22$  m at 27 June 0838 UTC, and b)  $-19.49$  m at  
 245 26 June 1124 UTC. Lines represent 1 s averaged wind vectors (scaled to the distance covered in 25  
 246 sec) at 8 m (black solid), 5 m (black dashed), 3 m (white solid) and 2 m (white dashed) a.g.l. at the  
 247 measurement location (white circle) respectively. The thick white line represents data excluded due to  
 248 the road.

249 The temporal evolutions of ST and AT fluctuations at different heights are then compared in  
 250 Fig. 4. The ST is the average across the scalar footprint (Eqs. 2) of the 2 m CSAT with a cut-off of  
 251 10% of the maximum value of the scalar footprint function. Fig. 4 shows that AT and STs are highly  
 252 cross-correlated and AT lags ST since the footprint is upstream: when the surface is cold the air starts  
 253 to cool and when the surface is warm the air starts to warm. Also, the AT at a lower altitude shows  
 254 more small scales compared to the ST. This is due to the fact that the ST is spatially averaged across  
 255 the footprint and not as affected by small scales as the surface has larger thermal mass. Comparing  
 256 Figs. 4a and 4b reveals that both ST and AT show more small scale fluctuations as the boundary layer  
 257 becomes more unstable. Similar results are obtained for all other stationary conditions.



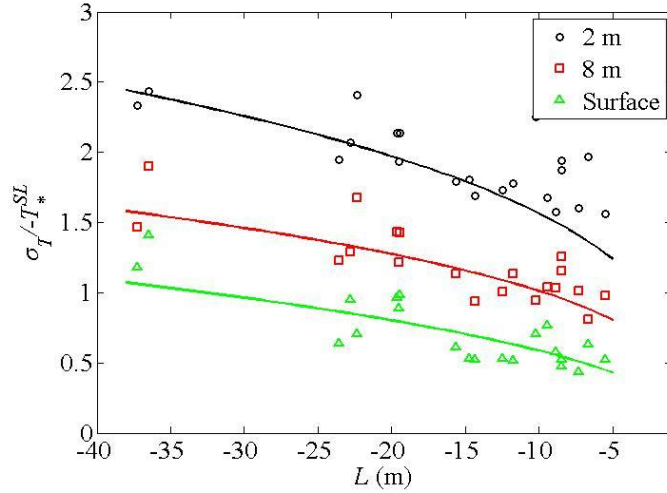
258

259 Figure 4. Time series of AT (colour bar) and footprint-averaged ST (bar plot) for  $L =$  a) -10.22 m at  
 260 27 June 0833-0838 UTC and b) -19.49 m at 26 June 1122-1127 UTC. ATs were vertically  
 261 interpolated using spline interpolation. The footprint is the area with greater than 10% of the  
 262 maximum value of the scalar footprint function of the 2 m CSAT.

263

264 Figure 5 shows temperature standard deviations normalized by the surface layer temperature  
 265 scale,  $T_*^{SL}$ , for all stationary periods. Normalized  $\sigma_{T_a}$  for 2 and 8 m a.g.l. decrease with increasing  
 266 height and stability closely following the surface layer similarity theory,  

$$\sigma_{T_a}/T_*^{SL} = -0.95(-z/L)^{-1/3}$$
 (Wyngaard et al., 1971).  $\sigma_{T_s}$  is smaller than  $\sigma_{T_a}$  at 8 m a.g.l. and can  
 267 be fit as  $\sigma_{T_s}/T_*^{SL} = -0.36(-\zeta)^{-0.39}$ . Direct numerical simulations of the solid-fluid coupled turbulent  
 268 heat transfer without buoyancy forcing term by Tiselj et al. (2001) showed that  $\sigma_{T_s}$  depends on the  
 269 solid thickness and the thermal properties of solid and fluid. They have characterized this  
 270 phenomenon by the thermal activity ratio,  $TAR = \frac{k_a}{k_g} \sqrt{\frac{\alpha_g}{\alpha_a}}$ , where  $k_a$  and  $\alpha_a$  are thermal conductivity  
 271 and thermal diffusivity of fluid. They found that a fluid-solid combination with low  $TAR$  does not  
 272 allow imprints of fluid temperature fluctuation on the solid surface. Balick et al. (2003) also found a  
 273 similar parameter for a coupled land-atmosphere heat transfer model. For our measurement site,  
 274 assuming  $k_a = 0.025 \text{ W m}^{-1} \text{ K}^{-1}$  and  $\alpha_a = 20 \text{ mm}^2 \text{ s}^{-1}$  and homogeneous clay soil with 40% volumetric  
 275 water content,  $TAR = 0.0044$ . Under these conditions according to Tiselj et al. (2001)  $\sigma_{T_s}$  would be  
 276 less than 1% of its iso-flux counterpart that corresponds to  $TAR \rightarrow \infty$ . Though our measurements  
 277 seem to overestimate  $\sigma_{T_s}$ , field experiment and DNS cannot be directly compared since the DNS  
 278 simulation ignored buoyancy term in the Navier-Stokes equations.

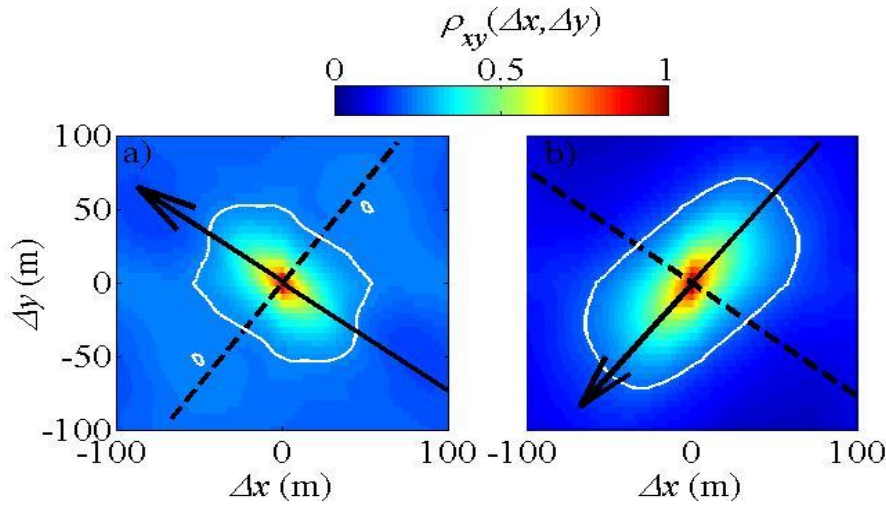


279

280 Figure 5. Normalized variance of ST and AT as a function of  $L$ . The markers are measurements for  
 281 the periods in Table 1, the black and red solid lines are fitted according to the surface layer similarity  
 282 theory  $\sigma_{Ta} / T_*^{SL} = -0.95(-z/L)^{-1/3}$  and the green line is the fit to the ST fluctuation:  $\sigma_{Ts} / T_*^{SL} =$   
 283  $0.36(-\zeta)^{-0.39}$ .

284 c. Spatial scale of surface temperature structures

285 The spatial scale of ST structures (as seen in Fig. 3) was then studied by considering the  
 286 spatial correlation for each image using  $\rho_{xy}(\Delta x, \Delta y, t) = \frac{\overline{T_s'(x, y, t) T_s'(x + \Delta x, y + \Delta y, t)}}{\sigma_{T_s}^2}$ , where the overbar  
 287 indicates a spatial average. Figure 9 shows the temporal average of the spatial correlation of the ST  
 288 structures ( $\rho_{xy}(\Delta x, \Delta y) = \langle \rho_{xy}(\Delta x, \Delta y, t) \rangle$ ) for  $L =$  (a) -10.22 m, and (b) -19.49 m. The ST  
 289 correlation structures are shaped as ellipsoids with the major axis aligned with the streamwise  
 290 direction.

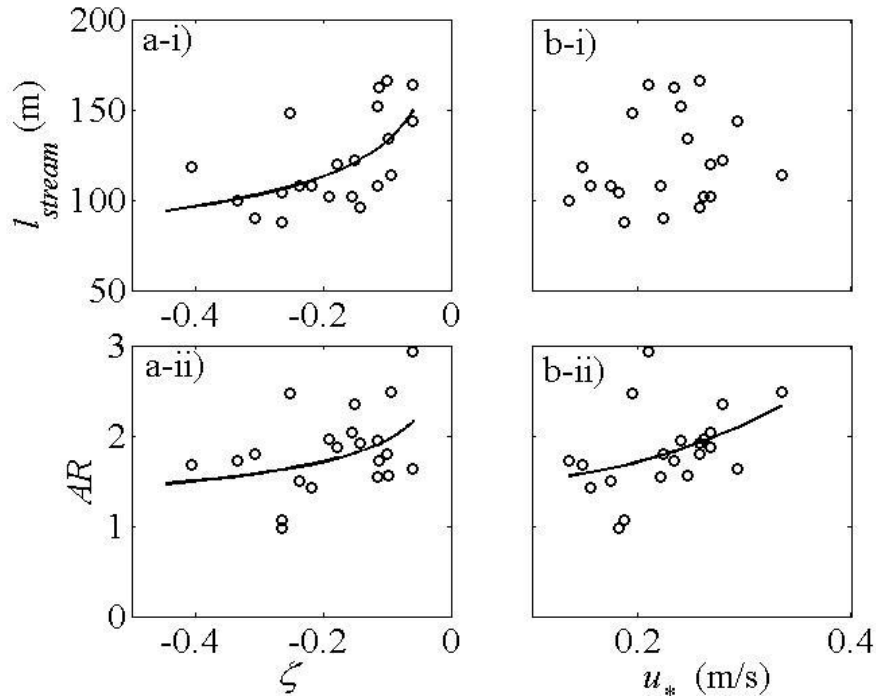


291



292 Figure 6. Mean spatial correlation of ST for  $L =$  (a) -10.22 m, and (b) -19.49 m (in the camera  
 293 coordinate system). The solid and broken black lines indicate averaged streamwise and spanwise  
 294 directions over 2, 3, 5 and 8 m a.g.l., respectively. The white contour line indicates a correlation of  
 295 0.25.

296 The spatial properties of coherent structures in a boundary layer flow depend on the shear and  
 297 the buoyancy. For a shear dominated boundary layer, the structures become elongated in the wind  
 298 direction and streaky, whereas for a buoyancy dominated boundary layer, they become more circular.  
 299 We consider  $u_*$  as a measure of shear and  $\zeta$  as a measure of relative strength of buoyancy over shear  
 300 to study their effect on the ST structures. Figure 7 shows (i) the streamwise correlation length ( $l_{stream}$ )  
 301 and (ii) the aspect ratio ( $AR = l_{stream}/l_{span}$ , where  $l_{span}$  is the spanwise correlation length) against  $\zeta$  and  
 302  $u_*$  for all stationary periods. The correlation length is defined as twice the distance from the centre  
 303 where the correlation becomes 0.25 in the streamwise and spanwise directions (Fig. 6). With  
 304 increasing stability the structures become longer. Thus the  $AR$  is close to unity for the more unstable  
 305 cases and larger than unity for the less unstable cases.  $l_{stream}$  does not show any recognizable trend  
 306 against  $u_*$ , but the  $AR$  increase from 1.5 for small  $u_*$  to more than 2 for larger  $u_*$ . Wilczak and  
 307 Tillman (1980) reported similar streamwise sizes of coherent structures based on the time traces of  
 308 AT at 4 m a.g.l..

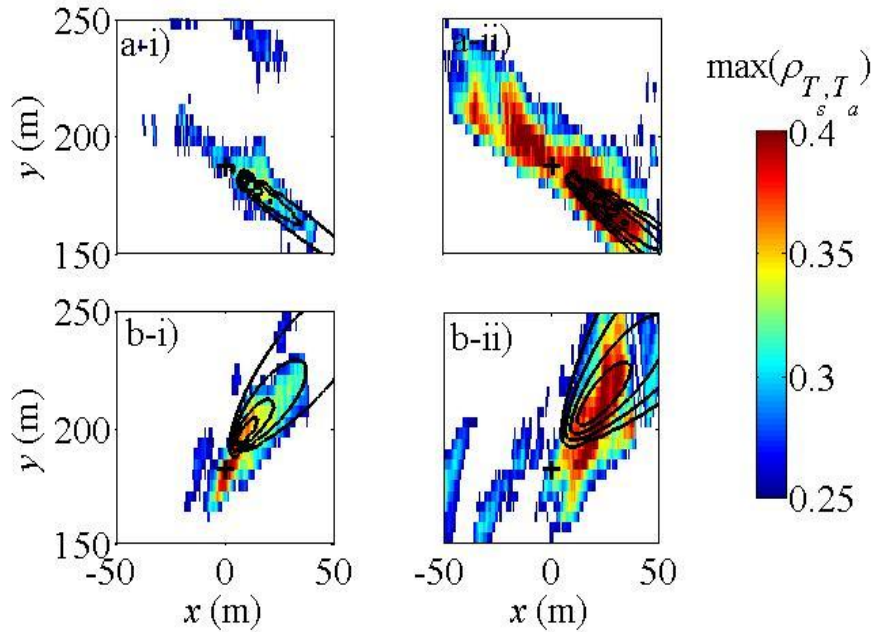


309  
 310 Figure 7. (i) Streamwise correlation length  $l_{stream}$  and (ii) aspect ratio  $AR$  of the mean ST structure with  
 311 (a)  $\zeta$  and (b)  $u_*$ . Markers represent the measurements and solid lines represent fits:  $l_{stream} =$

312  $78.03(-\zeta)^{-0.23}$ ,  $AR = 1.26(-\zeta)^{-0.19}$ ,  $AR = 11.43u_*^2 - 1.5u_* + 1.55$  with 48.6%, 28.0% and 27.7%  
 313 coefficient of determination respectively. No trend was observed and no line was fit for b-i.

#### 314 d. Surface and air temperature correlation

315 Since the footprint-averaged ST is correlated with AT (Fig. 4), spatial maps of cross-  
 316 correlation between ST and AT were generated using  $\rho_{T_s, T_a}(x, y, \Delta t) = \frac{\langle T_s'(x, y, t) T_a'(x_o, y_o, t + \Delta t) \rangle}{\sigma_{T_s} \sigma_{T_a}}$ , where  
 317  $x_o$  and  $y_o$  are the coordinates of the sonic tower and the two vectors are lagged by up to  $\Delta t = 60$  sec.  
 318 To reduce noise in the cross-correlation maps, an ensemble average of three cross-correlation maps  
 319 for each 10 min interval in a 30 min stationary period was computed. Spatial maps of maximum  
 320 cross-correlations between ST and AT at (i) 2 m and (ii) 8 m a.g.l. are shown in Fig. 8. The region of  
 321 maximum cross-correlation between ST and AT is aligned with the wind. The upwind correlation  
 322 region and the scalar footprint function show significant overlap (however, note the footprint  
 323 obviously only extends upwind while the correlation extends upwind and downwind). Specifically,  
 324 the cross-wind spread for the maximum correlation region is similar to that of the footprint function  
 325 which was modelled by a Gaussian distribution with a standard deviation of the wind direction (Eq.  
 326 2c). The maximum correlation coefficient, size of the correlation region, and the footprint increase  
 327 when the 8 m AT is correlated with the ST. Similar trends are also observed for the other stationary  
 328 periods.



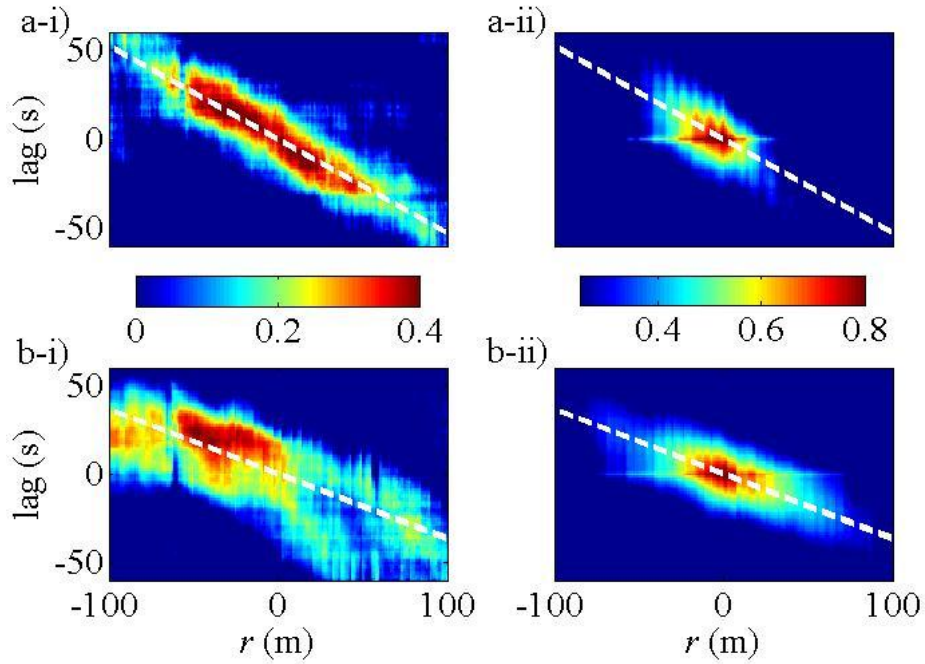
329

330 Figure 8. Thirty minute maximum cross-correlation between ST and AT at (i) 2 m and (ii) 8 m with  
 331 scalar footprint model (black contours) for  $L =$  (a) -10.22 m, and (b) -19.49 m. White pixels represent

332 ST-AT correlation less than 0.25 or unreasonable lags (absolute lag greater than 60 s). The black  
 333 contour line represents 10, 25, 50 and 75% of the maximum of scalar footprint function. The black +  
 334 sign marks the location of the sonic tower ( $x_o = 0.4$  m and  $y_o = 185$  m).

335 Along the wind direction cross-correlations between the AT at 8 m a.g.l. and the lagged ST  
 336 (Figs. 8-ii) are then plotted in Figs. 9-i. Here, positive  $r$  indicates the downwind direction and positive  
 337 lags indicate that the surface is preceding the air and vice versa. The largest cross-correlations for the  
 338 upwind (downwind) correlation region occur at a positive (negative) lag (shown in Figs. 9-i). Thus the  
 339 upwind ST is affecting the AT at the measurement location and the AT at the measurement location is  
 340 affecting the downwind ST, consistent with Garai and Kleissl (2011). Cross-correlations between ST  
 341 along the wind direction are shown in Figs. 9-ii as calculated using  $\rho_{T_s, T_s}(r, \Delta t; x_*, y_*) =$   
 342  $\frac{\langle T_s'(x_* + r \cos \theta, y_* + r \sin \theta, t + \Delta t) T_s'(x_*, y_*, t) \rangle}{\sigma_{T_s}^2}$ , where  $x_*, y_*$  and  $\theta$  are arbitrary coordinates in the image and  
 343 wind direction. To reduce the noise of the ST-ST cross-correlation, ensemble averages from 15  
 344 different  $(x_*, y_*)$  positions were computed. Note the distinction between these cross-correlations  
 345 versus the spatial correlations  $\rho_{xy}(\Delta x, \Delta y, t)$  described in Section 3c; the former ‘tracks’ ST  
 346 structures by co-varying space ( $r$ ) and time ( $\Delta t$ ), while the latter correlates structures that are not time  
 347 shifted across space. Therefore,  $\rho_{xy}(\Delta x, \Delta y, t)$  represents the typical spatial extent of ST structures at  
 348 a given time and  $\rho_{T_s, T_s}(r, \Delta t; x_*, y_*)$  represents the spatio-temporal region of influence of a given  
 349 structure. If a structure remained unchanged as it moves across the image,  $\rho_{T_s, T_s}(r, \Delta t; x_*, y_*)$  would  
 350 be large.

351 For ST-ST correlations, a positive lag indicates that the upwind ST is preceded by downwind  
 352 ST. The value of ST-ST cross-correlations in Figs. 9-ii are larger compared to AT-ST cross-  
 353 correlations in Fig. 9-i as the latter is calculated between two different variables and heights. Since the  
 354 spatial extent of the AT-ST region of large correlation depends on the AT measurement height, it is  
 355 not useful to compare quantitatively the spatial extent of the high correlation region for AT-ST and  
 356 ST-ST at a given stability. Qualitatively, as the stability of the boundary layer increases, the spatial  
 357 extent of high AT-ST and ST-ST correlation region increases. A less unstable boundary layer will  
 358 contain longer turbulence structures which is manifested in the larger footprints in Fig. 9-i. The AT-  
 359 ST and ST-ST correlation graphs allow tracking the advection speed of the structures responsible for  
 360 land-atmosphere exchange.



361

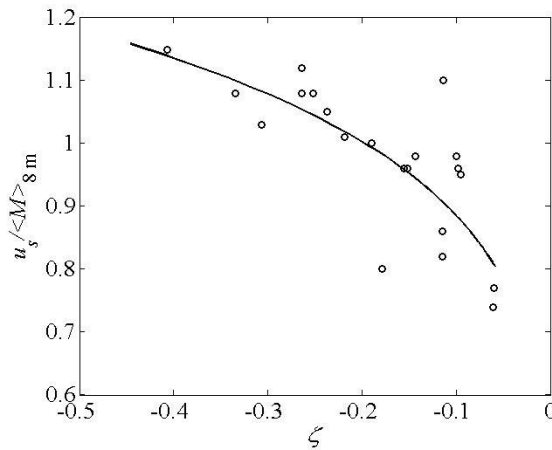
362 Figure 9. Left panels: Cross-correlation between AT at 8 m with ST along the 8 m wind direction at  
 363 different lags. Right panels: Cross-correlation amongst STs along the 8 m wind direction at different  
 364 lags. (a)  $L = -10.22$  m, and (b)  $L = -19.49$  m. The white dashed line represents the slope of the cross-  
 365 correlation area.

366 e. Advection speed of the surface temperature structures

367 The slopes of AT-ST and ST-ST temperatures cross-correlation surfaces show similar values  
 368 for a given stationary period, thus signifying the advective nature of the surface temperature coherent  
 369 structures. Hence, the slope of the cross-correlation in the lag-distance plot (Fig. 9) indicates the  
 370 advection speed  $u_s$  of the ST structures (or rather the turbulent coherent structures that leave an  
 371 imprint on the surface) along the wind direction. The estimated advection speeds for all stationary  
 372 periods are plotted in Fig. 10. The scatter in the plot is mostly due to the uncertainty in estimating the  
 373 slope; for some wind directions the high correlation region is discontinuous (as seen in Figure 8b-ii,  
 374 9b-i) due to surface heterogeneity. The advection speeds are similar to the wind speed at 8 m a.g.l.  
 375 with a decreasing trend in less unstable conditions.

376 Wilczak and Tillman (1980) also reported that the speeds of surface layer plumes are greater  
 377 than wind speed at 4 m a.g.l. with a small decreasing trend with stability. As the surface layer  
 378 becomes less unstable, the strength of buoyant production decreases compared to shear production,  
 379 resulting in less turbulent mixing. This causes a larger vertical gradient of horizontal wind speed in  
 380 the upper part of the surface layer and also a smaller effective plume height. The advection speed, i.e.  
 381 the mean wind speed over the height of the surface layer plume, should be identical to  $u_s$  of ST

382 coherent structures. Thus, with increase in the stability of the boundary layer the  $u_s$  decreases  
 383 compared to the wind speed at a sufficiently large altitude (e.g. 8 m a.g.l. in this case). Also as seen in  
 384 Figs. 2-c, except for 25 June the mixed layer wind speed is similar to the wind speed at 8 m a.g.l.  
 385 Consequently, one can conclude that  $u_s$  is similar to the mixed layer wind speed. This is consistent  
 386 with Katul et al. (1998) and Renno et al. (2004) who – in the absence of thermal imagery - resorted to  
 387 more elaborate spectral analysis to suggest that ST structures are caused by mixed layer turbulence.



388

389 Figure 10. Advection velocity of the ST structures (determined from Fig. 9) versus the 8 m wind  
 390 speed as a function of  $\zeta$ . Markers represent the measurements and the solid line represents the fit

391 equation  $u_s / \langle M \rangle_{8m} = 1.34(-\zeta)^{0.18}$  with 57.1% coefficient of determination.

### 392 f. Conditional averaging of ejection events

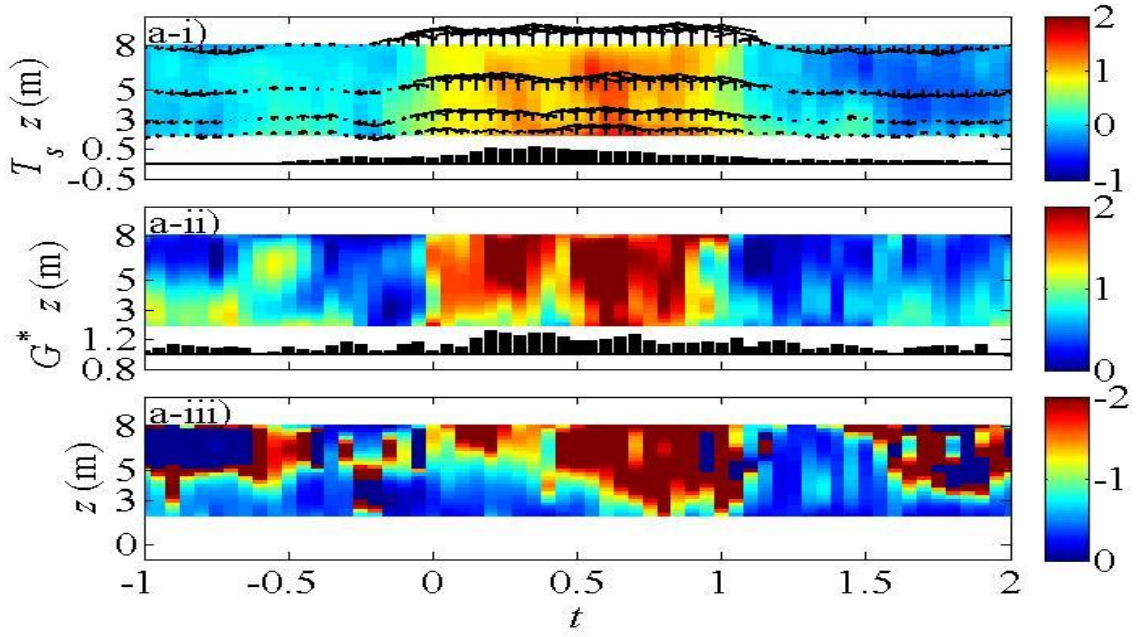
393 To study the coupling between ST and near surface coherent structures in more detail,  
 394 conditional averaging was employed. Events are classified as strong ejection events if  $w'T_a'_{8m} >$   
 395  $0.5\langle w'T_a' \rangle_{8m}$ ,  $w'$  is positive, and the minimum duration of the event is 3 s. Also, if two consecutive  
 396 events are separated by less than 5 s, they are merged into a single event. Estimated events are then  
 397 verified by visual inspection of the time series to ensure no false identification. These criteria result in  
 398 20 to 30 ejection events per stationary period with time scales ranging from 3 s to 45 s. The events  
 399 cover around 20 to 25% of each 30 min stationary period, but are responsible for 60 to 70% of the  
 400 sensible heat flux. Since the duration of each ejection event is different, time was normalized by the  
 401 individual ejection time scale such that  $t = 0$  and 1 indicates the start and end of the ejection event at 8  
 402 m a.g.l. respectively.

403 The ejection event is initiated by surface heating (Fig. 11-i). Since net radiation is nearly  
 404 constant during the short time frame of the event, the increase in ground heat flux associated with  
 405 surface heating has to be balanced by decreases in the convective fluxes. Thus before the ejection  
 406 event,  $w'T_a'$  is small. During the ejection event (Fig. 11-i) the warm air rises due to buoyancy,

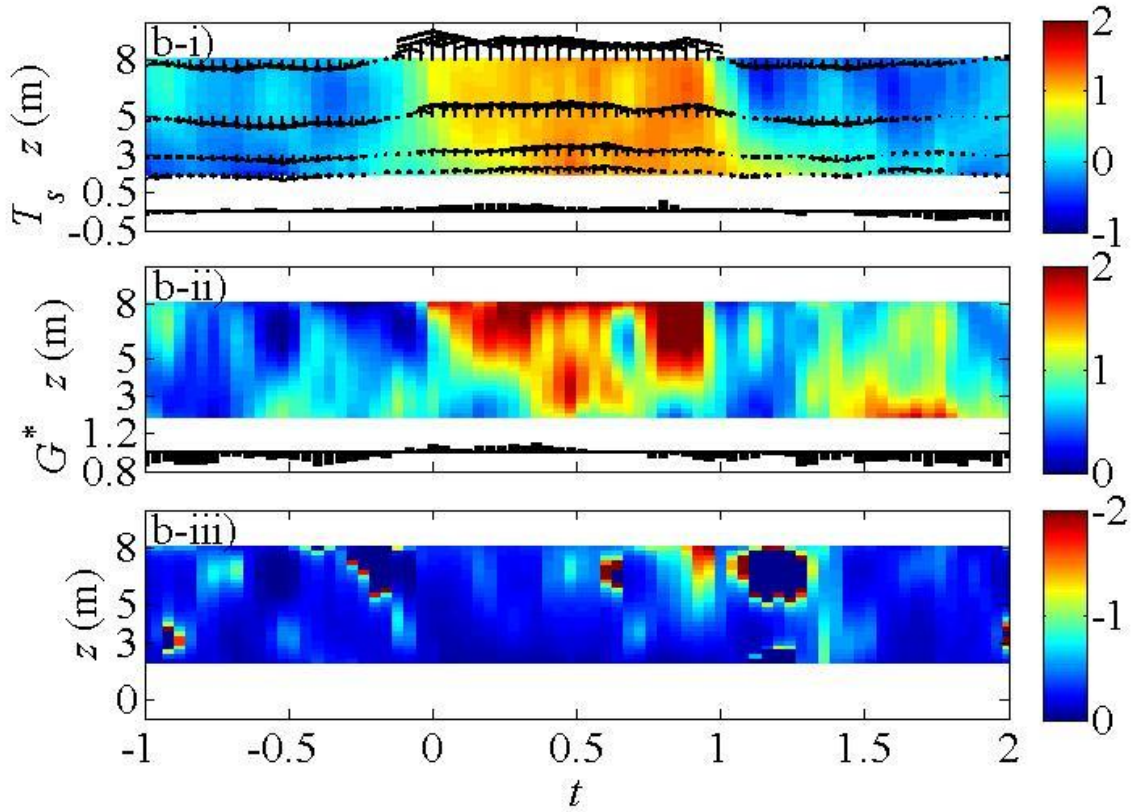
407 forming a surface layer plume. The majority of the vertical heat flux occurs during the ejection events  
408 (Fig. 11-ii) and buoyant production increases compared to shear production (Fig. 11-iii). After the  
409 ejection event, a downward flow of cold air occurs as a sweep event. The large convective heat flux  
410 during the ejection leads to cooling of the surface and as a result the ground heat flux decreases until  
411 the end of the sweep event. Also, note that though AT shows a ramp-like pattern (AT remains almost  
412 constant during the sweep, gradually increases during the sweep to ejection transition, attains  
413 maximum at the ejection and drops sharply during the ejection to sweep transition), the change in ST  
414 is smoother (gradual increase and decrease during sweep to ejection and to sweep events). This might  
415 be attributed to the higher thermal inertia of the surface compared to the air, so that small scale  
416 variations average out over the surface.

417         Though AT and ST follow similar trends, there is a time lag; the ST reaches its maximum  
418 before the AT and its minimum after the AT consistent with Garai & Kleissl (2011). Also, from Figs.  
419 11-i, it is evident that the plumes are slightly tilted due to wind shear. Since the shear production  
420 decreases more rapidly with height than buoyant production, the magnitude of  $Ri_f$  increases with  
421 height (Figs. 11-iii). Also, the magnitude of  $Ri_f$  during the ejection event decreases with increasing  
422 stability of the boundary layer. Similar results are obtained for the other stationary periods.

423         Although the magnitude of  $G$  depends on the thermal properties of the ground, the surface  
424 heat flux normalized by the mean,  $G^* = G/\langle G \rangle$ , will be independent of ground thermal properties as  
425 the ground conduction model is linear. Figs. 11-ii show that the ejection and sweep events cause  
426 variations of up to 0.3 times the mean ground heat flux.



427



428

429 Figure 11. Conditional average of ejection events occurring for  $L =$  (a)  $-10.22$  m, and (b)  $-19.49$  m. (i)  
 430 AT (colour), and ST (bars), both normalized by  $-T_*^{SL}$ . Vertical velocity vectors are overlaid (largest  
 431 vector corresponds to  $0.4 \text{ m s}^{-1}$ ). To convert ST to a time series, Taylor's frozen turbulence hypothesis  
 432 was applied using the advection speed of ST structures (Fig. 9). (ii)  $w'T_a'$  normalized by  $\langle w'T_a' \rangle_{2m}$   
 433 (colour) and modelled ground heat flux normalized by mean ground heat flux ( $G^*$ , bars). (iii)  $Ri_f$ . The  
 434 time axes are normalized such that  $t = 0$  and  $1$  correspond to the start and the end of the ejection event

435 at 8 m a.g.l., respectively. Note that the ST is not from the footprint of AT, but rather the temperature  
436 directly below the AT measurements.

## 437 4. Discussion and conclusion

438 Coupled land-atmosphere heat transfer was examined using lower surface layer eddy  
439 covariance measurements and IR surface temperature imagery for a range of unstable conditions in  
440 the CBL. The sequential IR images of ST show that temperature patterns in the surface grow,  
441 combine with each other and move along the wind. These ST patterns can be interpreted to be the  
442 imprints of turbulent coherent structures on the surface in a CBL (Derksen, 1974; Schols et al. 1985;  
443 Paw U et al. 1992; Katul et al. 1998; Balick et al. 2003; Ballard et al. 2004; Renno et al. 2004; Vogt,  
444 2008; Christen and Voogt, 2009, 2010; Christen et al. 2011; Garai & Kleissl, 2011). When ST  
445 standard deviations are compared with AT standard deviations, they follow a similar trend with  
446 respect to stability and the former is smaller than the latter at 8 m a.g.l. The normalized  $\sigma_{T_S}$  gives a  
447 similar power law exponent (0.39) compared to surface layer similarity theory (Wyngaard et al.,  
448 1971); the coefficient of proportionality differs significantly (for our data, 0.36), but it should depend  
449 on the surface thermal property (Tiselj et al., 2001; Balick et al., 2003). Different  $\sigma_{T_S}$  over different  
450 surfaces ( $\sigma_{T_S}$  over metallic roofs > lawns > roads > building walls) was also reported by Christen et  
451 al. (2012) for an urban measurement site.

452 Cross-correlating ST and AT, the maximum correlation region aligns with the wind direction.  
453 The cross-wind span of the correlation region depends on the standard deviation of the wind direction.  
454 The upwind correlation region corresponds well to the scalar footprint formulated from the footprint  
455 by Hsieh et al. (2000). The lag associated with the maximum correlation reveals that the upwind ST  
456 fluctuations affect the AT fluctuations at the measurement tower and the AT fluctuations at the  
457 measurement tower affect the downwind ST fluctuations. This indicates that vertically coherent  
458 structures advect smaller and larger temperature fluid downwind and these structures leave a  
459 temperature footprint on the surface. The correlation between footprint-averaged ST with AT  
460 increases from 2 m to 8 m. All these observations point to the surface temperature fluctuations being  
461 caused by turbulent coherent structures in the atmospheric boundary layer.

462 The mean streamwise size of the ST structures (or rather the turbulent coherent structures that  
463 leave an imprint on the surface) decreases with  $\zeta$ . The AR of the structures increases with both  $u_*$  and  
464  $\zeta$ . Wilczak and Tillman (1980) also reported similar values of turbulent structure size and their  
465 advection speed in CBL by considering time trace of AT at 4 m a.g.l.. These findings further  
466 substantiate that the ST patterns reflect common properties of turbulent coherent structures in the  
467 boundary layer. More unstable flows cause more circular and shorter coherent structures while more  
468 neutral flows give rise to longer, streaky patterns.



469 The advection speed of the structures was of the order of wind speed at 8 m a.g.l. and it  
470 decreased with stability. The mixed layer wind speed was almost the same as the wind speed at 8 m  
471 a.g.l.. Similar results were reported by Christen and Voogt (2009, 2010) and Garai and Kleissl (2011).  
472 Katul et al. (1998) and Renno et al. (2004) inferred that high frequency ST fluctuations were caused  
473 by mixed layer turbulence.

474 The ST coherent structures are finally interpreted in the context of the surface renewal (SR)  
475 method. While the Lagrangian concept of the SR method cannot be conclusively demonstrated in the  
476 Eulerian measurement framework, the observations give rise to the following interaction between  
477 coherent structures and the surface. During the sweep event, a cold air parcel descends and the surface  
478 cools due to enhanced temperature gradient and heat transfer between surface and air. The cooler  
479 surface results in a smaller ground heat flux during this time (Figs. 11-i and ii;  $t > 1$  or  $-1 < t < -0.5$ ).  
480 As the air parcel remains in contact with the surface it warms gradually, reducing heat transfer  
481 between the surface and the air. The ground heat flux increases during this time. Thus, the surface  
482 starts to warm (Figs. 11-i and ii;  $-0.5 < t < 0$ ). As the air parcel warms up, it gains buoyancy (Figs. 11-  
483 iii). With sufficient buoyancy (and possibly assisted by mixed layer turbulence) the air parcel ascends  
484 in an ejection event. During the initial period of the ejection event, the ground heat flux reaches a  
485 maximum (Figs. 11-i;  $0 < t < 0.5$ ). As the ejection event continues large heat transfer occurs between  
486 the surface and the air (Figs. 11-ii;  $0 < t < 0.5$ ). Afterwards the surface starts to cool and the ground  
487 heat flux starts to decrease (Figs. 11-ii;  $t > 0.5$ ).

488 In Garai & Kleissl (2011), we also analyzed ST structures during different phases of the SR  
489 cycle. In this study, with the larger camera field of view and availability of AT at different heights, we  
490 have successfully visualized SR events both in the surface layer and on the surface. However, due to  
491 the larger camera field of view in this study, a single image contains several SR events at different  
492 stages (Fig. 3). Thus the size of the ST structure for each individual SR event is averaged out when  
493 spatial correlation within an image is considered (Section 3c). While it cannot be demonstrated in this  
494 study, we expect the temporal evolution of the structure size to be similar as found in Garai and  
495 Kleissl (2011): during the ejection event there will be a large warm ST structure, during the sweep  
496 event there will be a large cold ST structure, at the transition from ejection to sweep there will be  
497 small patches of cold ST structures, and at the transition from sweep to ejection there will be small  
498 patches of warm ST structures. These ST structures grow, combine with each other and move along  
499 the higher altitude wind. Strong sweep events are followed by ejection events and the heat transfer  
500 mechanism repeats itself. We observed that the surface reaches maximum temperature before the air  
501 and minimum temperature after the air. The majority of heat transport occurs during the ejection event  
502 (about 60 to 70% of the total sensible heat flux), which also causes ground heat flux variations (about  
503 30% of the mean ground heat flux) through surface energy budget. Thus the turbulence induced

504 surface temperature variation should be accounted for in numerical models as they cause a  
505 considerable amount of surface energy budget anomaly.

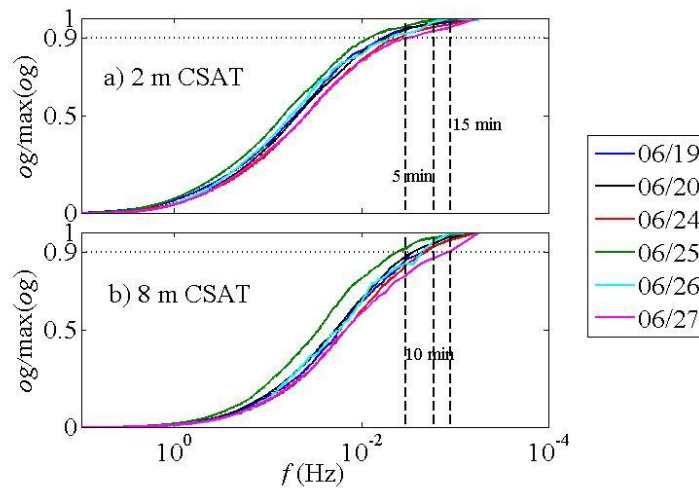
506

507 **Acknowledgements:** We are thankful to (i) Daniel Alexander from University of Utah, USA;  
508 Dr. Fabienne Lohou, Solene Derrien from Laboratoire d'Aérodynamique, Université de Toulouse, France;  
509 Dr. Arnold Moene, Anneke Van de Boer, Oscar Hartogensis from Wageningen University,  
510 Netherland for field assistance, data sharing and discussion; (ii) Peter Cottle and Anders Nottrott from  
511 University of California, San Diego for pre-experimental laboratory assistance and discussion about  
512 the data analysis respectively, (iii) BLLAST organizers, Marie Lothon, Fabienne Lohou and Eric  
513 Pardyjak for their hospitality during the experiment; (iv) funding from a NASA New Investigator  
514 Program award.

515

## 516 Appendix

517 The ogive function can be employed to estimate the sufficient averaging period for  
518 calculation of turbulent fluxes using the eddy-covariance method. Ogive ( $og_{w,X}(f_o)$ ) is a cumulative  
519 integral of the co-spectrum,  $Co_{w,X}$ , of a variable,  $X$ , with vertical velocity,  $w$ , starting with the highest  
520 frequency,  $f$ ,  $og_{w,X}(f_o) = \int_{\infty}^{f_o} Co_{w,X}(f)df$ . Ideally the ogive function increases during the integration  
521 from high frequency to small frequency, until reaching a constant value. Hence the period  
522 corresponding to the frequency at which the ogive reaches the constant value is considered to be  
523 sufficient to capture the largest turbulence scales. To improve the statistical significance and minimize  
524 the effect of diurnal cycles, twenty six 30 min segments for each clear days corresponding to 0600 –  
525 1900 UTC were used. It was found that a 5 min averaging period accounts for 90% and 85% of the  
526 maximum value of ogive for 2 m and 8 m CSATs respectively for the sensible heat flux (Fig. 12)  
527 and the momentum flux (not shown). Thus an averaging period of 5 min was selected.



528

529 Figure 12. The normalized ogive by its maximum value for heat flux calculation at 2 and 8 m CSAT  
 530 of all the clear days.

531

532 **References**

533 Ballard JR, Smith JA, Koenig GG (2004) Towards a high temporal frequency grass canopy  
 534 thermal IR model for background signatures. Proc SPIE 5431:251-259.

535 Balick LK, Jeffery CA, Henderson B (2003) Turbulence induced spatial variation of surface  
 536 temperature in high resolution thermal IR satellite imagery. Proc SPIE 4879:221-230.

537 Braaten DA, Shaw RH, Paw U KT (1993) Boundary-layer flow structures associated with  
 538 particle reentrainment. Boundary-Layer Meteorol 65:255-272.

539 Businger JA, Wyngaard JC, Izumi Y, Bradley EF (1971) Flux profile relationships in the  
 540 atmospheric surface layer. J Atmos Sci 28:181-189.

541 Campbell GS, Norman JM (1998) An introduction to environmental biophysics. Springer  
 542 Verlag, New York, USA, 286 pp.

543 Carslaw HS, Jaeger JC (1959) Conduction of heat in solids. Oxford University Press,  
 544 London, UK, 510 pp.

545 Castellvi F (2004) Combining surface renewal analysis and similarity theory: a new approach  
 546 for estimating sensible heat flux. Water Resour Res 40:W05201.

- 547 Castellvi F, Perez PJ, Ibanez M (2002) A method based on high-frequency temperature  
548 measurements to estimate the sensible heat flu avoiding the height dependence. *Water*  
549 *Resour Res* 38(6):1084.
- 550 Castellvi F, Snyder RL (2009) Combining the dissipation method and surface renewal  
551 analysis to estimate scalar fluxes from the time traces over rangeland grass near Ione  
552 (California). *Hydrol Process* 23:842-857.
- 553 Christen A, Meier F, Scherer D (2012) High-frequency fluctuations of surface temperatures  
554 in an urban environment, *Theor Appl Climatol* 108:301-324.
- 555 Christen A, Voogt JA (2009) Linking atmospheric turbulence and surface temperature  
556 fluctuations in a street canyon. Paper no. A3-6. The 7<sup>th</sup> International Conference on  
557 Urban Climate, Yokohoma, Japan.
- 558 Christen A, Voogt JA (2010) Inferring turbulent exchange process in an urban street canyon  
559 from high-frequency thermography. Paper no. J3A.3. 9<sup>th</sup> Symposium on the Urban  
560 Environment, Keystone, Colorado, USA.
- 561 Derksen DS (1974) Thermal infrared pictures and the mapping of microclimate. *Neth J Agric*  
562 *Sci* 22:119-132.
- 563 Foken T, Wimmer F, Mauder M, Thomas C, Liebethal C (2006) Some aspects of the energy  
564 balance closure problem. *Atmos Chem Phys* 6:4395-4402.
- 565 Gao W, Shaw RH, Paw U KT (1989) Observation of organized structure in turbulent flow  
566 within and above a forest canopy. *Boundary-Layer Meteorol* 47:349-377.
- 567 Garai A, Kleissl J (2011) Air and surface temperature coupling in the convective atmospheric  
568 boundary layer. *J Atmos Sci* 68:2945-2954.
- 569 Gurka R, Liberzon A, Hestroni G (2004) Detecting coherent patterns in a flume by using PIV  
570 and IR imaging techniques. *Exp Fluids* 37:230-236.
- 571 Hestroni G, Rozenblit R (1994) Heat transfer to a liquid-solid mixture in a flume. *Int J*  
572 *Multiphase Flow* 20:671-689.

- 573 Hestroni G, Kowalewski TA, Hu B, Mosyak A (2001) Tracking of coherent thermal  
574 structures on a heated wall by means of infrared thermography. *Exp Fluids* 30:286-  
575 294.
- 576 Howard LN (1966) Convection at high Rayleigh number. *Proceedings of the 11<sup>th</sup>*  
577 *International Congress on Applied Mechanics*, H. Görtler, Ed., Springer-Verlag,  
578 1109-1115.
- 579 Hsieh C-I, Katul GG, Chi T (2000) An approximate analytical model for footprint estimation  
580 of scalar fluxes in thermally stratified atmospheric flows. *Adv Water Resour* 23:765-  
581 772.
- 582 Kaimal JC, Businger JA (1970) Case studies of a convective plume and a dust devil. *J Appl*  
583 *Meteorol* 9:612-620.
- 584 Kaimal JC, Wyngard JC, Haugen DA, Cote OR, Izumi Y (1976) Turbulence structure in the  
585 convective boundary layer. *J Atmos Sci* 33:2152-2169.
- 586 Katul GG, Schieldge J, Hsieh C-I, Vidakovic B (1998) Skin temperature perturbations  
587 induced by surface layer turbulence above a grass surface. *Water Resour Res*  
588 34:1265-1274.
- 589 Kormann R, Meixner FX (2001) An analytical footprint model for non-neutral stratification.  
590 *Boundary-Layer Meteorol* 99:207-224.
- 591 Lothon M, Lohou F, Durand P, Couvreux Sr. F, Hartogensis OK, Legain D, Pardyjak E, Pino  
592 D, Reuder J, Vilà Guerau de Arellano J, Alexander D, Augustin P, Bazile E,  
593 Bezombes Y, Blay E, van de Boer A, Boichard JL, de Coster O, Cuxart J, Dabas A,  
594 Darbieu C, Deboudt K, Delbarre H, Derrien S, Faloona I, Flament P, Fourmentin M,  
595 Garai A, Gibert F, Gioli B, Graf A, Groebner J, Guichard F, Jonassen M, van de  
596 Kroonenberg A, Lenschow D, Martin S, Martinez D, Mastrorillo L, Moene A, Moulin  
597 E, Pietersen H, Piguët B, Pique E, Román-Cascón C, Said F, Sastre M, Seity Y,  
598 Steeneveld GJ, Toscano P, Traullé O, Tzanos D, Wacker S, Yagüe C (2012) The  
599 boundary layer late afternoon and sunset turbulence 2011 field experiment. Paper no.  
600 14B.1. 20<sup>th</sup> Symposium on Boundary Layers and Turbulence, Boston, Massachusetts,  
601 USA.
- 602 Oke TR (1987) *Boundary layer climates*. Methuen, London, UK, 435 pp.

603 Paw U KT, Brunet Y, Collineau S, Shaw RH, Maitani T, Qiu J, Hipps L (1992) On coherent  
604 structures in turbulence above and within agricultural plant canopies. *Agric For*  
605 *Meteorol* 61:55-68.

606 Paw U KT, Qiu J, Su H-B, Watanabe T, Brunet Y (1995) Surface renewal analysis: a new  
607 method to obtain scalar fluxes. *Agric For Meteorol* 74:119-137.

608 Raupach MR, Finnigan JJ, Brunet Y (1996) Coherent eddies and turbulence in vegetation  
609 canopies: the mixing-layer analogy. *Boundary-Layer Meteorol* 78:351-382.

610 Renno NO, Abreu VJ, Koch J, Smith PH, Hartogensis OK, De Bruin HAR, Burose D, Delory  
611 GT, Farrell WM, Watts CJ, Garatuza J, Parker M, Carswell A (2004) MATADOR  
612 2002: A pilot experiment on convective plumes and dust devils. *J Geophys Res*  
613 109:E07001.

614 Schols JLJ (1984) The detection and measurement of turbulent structures in the atmospheric  
615 surface layer. *Boundary-Layer Meteorol* 29:39-58.

616 Schols JLJ, Jansen AE, Krom JG (1985) Characteristics of turbulent structures in the unstable  
617 atmospheric surface layer. *Boundary-Layer Meteorol* 33:173-196.

618 Snyder RL, Spano D, Paw U KT (1996) Surface renewal analysis for sensible and latent heat  
619 flux density. *Boundary-Layer Meteorol* 77:249-266.

620 Spano D, Snyder RL, Duce P, Paw U KT (1997) Surface renewal analysis for sensible heat  
621 flux density using structure functions. *Agric For Meteorol* 86:259-271.

622 Spano D, Snyder RL, Duce P, and Paw U KT (2000) Estimating sensible and latent heat flux  
623 densities from grapevine canopies using surface renewal. *Agric For Meteorol*  
624 104:171-183.

625 Sparrow EM, Husar RB, Goldstein RJ (1970) Observations and other characteristics of  
626 thermals. *J Fluid Mech* 41:793-800.

627 Tiselj I, Bergant R, Makov B, Bajsić I, Hestroni G (2001) DNS of turbulent heat transfer in  
628 channel flow with heat conduction in the solid wall. *J Heat Transfer* 123:849-857.

629 Townsend AA (1959) Temperature fluctuation over a heated horizontal surface. *Fluid Mech*  
630 5:209-241.

- 631 Vogt R (2008) Visualisation of turbulent exchange using a thermal camera. Paper no. 8B.1.  
632 18<sup>th</sup> Symposium on Boundary Layer and Turbulence, Stockholm, Sweden.
- 633 Wilczak JM, Businger JA (1983) Thermally indirect motions in the convective atmospheric  
634 boundary layer. *J Atmos Sci* 40:343-358.
- 635 Wilczak JM, Tillman JE (1980) The three-dimensional structure of convection in the  
636 atmospheric surface layer. *J Atmos Sci* 37:2424-2443.
- 637 Wilczak JM, Oncley SP, Stage SA (2001) Sonic anemometer tilt correction algorithms.  
638 *Boundary-Layer Meteorol* 99:127-150.
- 639 Wyngaard JC, Cote OR, Izumi Y (1971) Local free convection, similarity and the budgets of  
640 shear stress and heat flux. *J Atmos Sci* 28:1171-1182.